

Galaxies going MAD: The Galaxy-Finder Comparison Project

Alexander Knebe^{1*}, Noam I. Libeskind², Frazer Pearce³, Peter Behroozi^{4,5,6},
Javier Casado¹, Klaus Dolag^{7,8}, Rosa Dominguez-Tenreiro¹, Pascal Elahi⁹,
Hanni Lux³, Stuart I. Muldrew³, Julian Onions³

¹*Departamento de Física Teórica, Módulo C-15, Facultad de Ciencias, Universidad Autónoma de Madrid, 28049 Cantoblanco, Madrid, Spain*

²*Leibniz Institut für Astrophysik, An der Sternwarte 16, 14482 Potsdam, Germany*

³*School of Physics & Astronomy, University of Nottingham, Nottingham, NG7 2RD, UK*

⁴*Kavli Institute for Particle Astrophysics and Cosmology, Stanford, CA 94309, USA*

⁵*Physics Department, Stanford University, Stanford, CA 94305, USA*

⁶*SLAC National Accelerator Laboratory, Menlo Park, CA 94025, USA*

⁷*Max-Planck Institut für Astrophysik, Karl-Schwarzschild Str. 1, D-85741 Garching, Germany*

⁸*University Observatory München, Scheinerstr. 1, 81679, München, Germany*

⁹*Key Laboratory for Research in Galaxies and Cosmology, Shanghai Astronomical Observatory, Shanghai 200030, China*

Accepted XXXX . Received XXXX; in original form XXXX

ABSTRACT

With the ever increasing size and complexity of fully self-consistent simulations of galaxy formation within the framework of the cosmic web, the demands upon object finders for these simulations has simultaneously grown. To this extent we initiated the Halo Finder Comparison Project that gathered together all the experts in the field and has so far led to two comparison papers, one for dark matter field haloes (Knebe et al. 2011), and one for dark matter subhaloes (Onions et al. 2012). However, as state-of-the-art simulation codes are perfectly capable of not only following the formation and evolution of dark matter but also account for baryonic physics, i.e. gas hydrodynamics, star formation, stellar feedback, etc., object finders should also be capable of taking these additional physical processes into consideration. Here we report – for the first time – on a comparison of codes as applied to the Constrained Local Universe Simulation (CLUES) of the formation of the Local Group which incorporates much of the physics relevant for galaxy formation. We compare both the properties of the three main galaxies in the simulation (representing the Milky Way, Andromeda, and M33) as well as their satellite populations for a variety of halo finders ranging from phase-space to velocity-space to spherical overdensity based codes, including also a mere baryonic object finder. We obtain agreement amongst codes comparable to (if not better than) our previous comparisons – at least for the total, dark, and stellar components of the objects. However, the diffuse gas content of the haloes shows great disparity, especially for low-mass satellite galaxies. This is primarily due to differences in the treatment of the thermal energy during the unbinding procedure. We acknowledge that the handling of gas in halo finders is something that needs to be dealt with carefully, and the precise treatment may depend sensitively upon the scientific problem being studied.

Key words: methods: N -body simulations – galaxies: haloes – galaxies: evolution – cosmology: theory – dark matter

1 INTRODUCTION

In a series of precursory papers (Knebe et al. 2011; Onions et al. 2012, see also Knebe et al., in prep.) we have compared and quantified the differences arising from the application of various halo finders to the same (dark matter only) data sets. The motivation for such comparisons is obvious: while past decades have seen great strides to better understand disparities in cosmological simulations stemming from different gravity (and hydrodynamics) solvers (e.g.

* E-mail: alexander.knebe@uam.es

Frenk et al. 1999; Knebe et al. 2000; O’Shea et al. 2005; Agertz et al. 2007; Heitmann et al. 2008; Tasker et al. 2008; Robertson et al. 2010; Springel 2010; Vazza et al. 2011) it was about time to initiate a similar project for object finders. To put it in a provocative way, if you are not only interested in the matter distribution in the universe, any simulation is only as good as the halo catalogue derived from it, especially at a time when we will have access to extremely large redshift surveys (just to name a few, BOSS, WiggleZ, eBOSS, BigBOSS, DESpec, PanSTARRS, DES, HSC, Euclid, WFIRST, etc.) against which the next generation of cosmological simulations (and the haloes/galaxies found in them) should and will be compared against.

However, all our previous comparisons solely focused on dark matter haloes and left aside any possible influence of the baryons. In this work we extend the comparison project to a cosmological simulation that not only models gravity, but simultaneously follows the evolution of the baryonic material by incorporating a self-consistent solution to the hydrodynamics. The simulation further includes star formation and stellar feedback, all explained in more detail in the subsequent Section 2. Please note that we are not trying to address the question of (disk) galaxy formation in this work, but rather aim at using one of these simulations to verify whether a halo finder applied to it will find the same (galactic) objects as any other halo finder. In particular, we will study both the larger (disk) galaxies as well as their respective satellite populations. To this extent we use a constrained zoom simulation of the Local Group of galaxies consisting of objects akin to the Milky Way (MW), the Andromeda galaxy (M31), and M33. This data forms part of the Constrained Local Universe (CLUES) project.¹

The questions to be addressed are plain and simple: while it is well established that baryonic physics alters the particulars of dark matter haloes and subhalo populations (Blumenthal et al. 1986; Tissera & Dominguez-Tenreiro 1998; Macciò et al. 2006; Oñorbe et al. 2007; Romano-Díaz et al. 2008, 2009; Libeskind et al. 2010; Duffy et al. 2010; Sommer-Larsen & Limousin 2010; Romano-Díaz et al. 2010; Schewtschenko & Macciò 2011; di Cintio et al. 2011; Governato et al. 2012; Zolotov et al. 2012; Brooks & Zolotov 2012; Di Cintio et al. 2012), there remains the question of how this will influence the performance of an object finder. Note that cold baryonic material tends to cluster more strongly than its dark matter counterpart due to the dissipative nature of the cooling process allowing for the disposal of energy via radiation. While star particles – generated on-the-fly during the simulation according to a physically motivated prescription that transforms cold gas into stars – only feel gravitational forces (like the dark matter particles), they nevertheless originate from compact, condensed regions. Additionally the gas particles themselves carry not only kinetic but also thermal energy giving rise to thermal pressure in the medium (specified by the adopted equation of state). At present, halo finders deal with these subtleties differently, with some properly accounting for the gas pressure and others ignoring it. Therefore, the fundamental question is, what will different halo/galaxy finders find when it comes to simulations including baryonic physics?

Here we compare a range of different (halo) finding techniques ranging from phase-space to velocity-space to spherical overdensity based codes, but also including a mere baryonic object finder. This naturally raises the question about the right approach to actually find galaxies. Should one hunt for dark matter haloes first and then characterize the galaxy residing in it? Or is it more

reasonable to initially locate galaxies and then identify their surrounding dark matter haloes? Our suite of object finders contains both methods of operation and we will hence learn about these different strategies, too.

2 THE DATA

We use the same simulation already presented in Libeskind et al. (2010); Gottlöber et al. (2010); Libeskind et al. (2011); Knebe et al. (2010); Libeskind et al. (2011); Knebe et al. (2011); di Cintio et al. (2011); Dayal & Libeskind (2012); Di Cintio et al. (2012) and refer the reader to these papers for a more exhaustive discussion and presentation of our constrained simulations of the Local Group that form part of the aforementioned CLUES project. We briefly summarise their main properties here for clarity.

2.1 Constrained Simulations of the Local Group

We choose to run our simulations using standard Λ CDM initial conditions, that assume a WMAP3 cosmology (Spergel et al. 2007), i.e. $\Omega_m = 0.24$, $\Omega_b = 0.042$, $\Omega_\Lambda = 0.76$. We use a normalisation of $\sigma_8 = 0.73$ and a $n = 0.95$ slope of the power spectrum. We used the treePM-SPH code GADGET2 (Springel 2005) to simulate the evolution of a cosmological box with side length of $L_{\text{box}} = 64h^{-1}\text{Mpc}$. Within this box we identified (in a lower-resolution run utilizing 1024^3 particles) the position of a model local group that closely resembles the real Local Group (cf. Libeskind et al. 2010). This Local Group has then been re-sampled with 64 times higher mass resolution in a region of $2h^{-1}\text{Mpc}$ about its centre giving a nominal resolution equivalent to 4096^3 particles, resulting in a mass resolution of $m_{\text{DM}} = 2.5 \times 10^5 h^{-1} M_\odot$ for the dark matter and $m_{\text{gas}} = 4.4 \times 10^4 h^{-1} M_\odot$ for the gas particles. The force resolution is $0.15h^{-1} \text{kpc}$.

For this particular study we focus on the gas dynamical smoothed particle hydrodynamics (SPH) simulation, in which we follow the feedback and star formation rules of Springel & Hernquist (2003): the interstellar medium (ISM) is modelled as a two phase medium composed of hot ambient gas and cold gas clouds in pressure equilibrium. The thermodynamic properties of the gas are computed in the presence of a uniform but evolving ultra-violet cosmic background generated from QSOs and AGNs and switched on at $z = 6$ (Haardt & Madau 1996). Cooling rates are calculated from a mixture of a primordial plasma composition. No metal dependent cooling is assumed, although the gas is metal enriched due to supernovae explosions. Molecular cooling below 10^4K is also ignored. Cold gas cloud formation by thermal instability, star formation, the evaporation of gas clouds, and the heating of ambient gas by supernova driven winds are assumed to all occur simultaneously.

To give a visual impression of our simulated Local Group we present in Fig. 1 a colour-coded density map of it as well as a zoom of the stellar disks of three main galaxies considered in this study. For more details we refer the reader to the CLUES web site or the aforementioned papers. But please note that the actual simulation is not up for debate here: the prime objective of this work is to compare objects finders and hence any reasonable simulation of galaxy formation might serve this purpose.

¹ <http://www.clues-project.org>

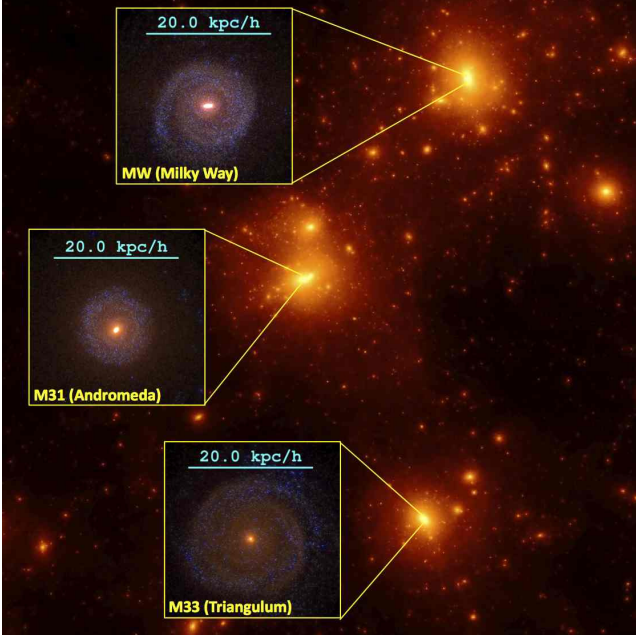


Figure 1. A graphical representation of the CLUES simulation data showing the three main galaxies considered in this study, i.e. M31, the MW and M33. In Section 4 the properties of those three main galaxies will be compared whereas Sections 5 and 6 focus on the satellite populations of M31 and the MW. *Image courtesy CLUES collaboration.*

2.2 Lighting up (Sub-)Haloes

The stellar population synthesis model STARDUST (see Devriendt et al. 1999, and references therein for a detailed description) has been used to derive luminosities from the stars formed in our simulation. This model computes the spectral energy distribution from the far-UV to the radio, for an instantaneous starburst of a given mass, age and metallicity. The stellar contribution to the total flux is calculated assuming a Kennicutt initial mass function (Kennicutt 1998).

3 THE CODES

Before (briefly) presenting the particulars of the codes, it is important to state that all of the participating codes are at various stages with respect to their capabilities of handling simulation data that includes not only (equal) mass dark matter particles, but also star and gas particles. For instance, SUBFIND with its careful treatment of the gas thermal properties, is the most advanced with respect to the simulation data at hand, whereas on the other hand ROCKSTAR required substantial post-processing as it treats all particles on a equal footing at present.

3.1 AHF (Knebe)

The halo finder AHF² (AMIGA Halo Finder) is a spherical over-density finder that identifies (isolated and sub-)haloes as described in Gill et al. (2004) as well as Knollmann & Knebe (2009). The initial particle lists are obtained by a rather elaborate scheme: for each subhalo the distance to its nearest more massive (sub-)halo is

calculated and all particles within a sphere of radius half this distance are considered prospective subhalo constituents. This list is then pruned by an iterative unbinding procedure using the (fixed) subhalo centre as given by the local density peak determined from an adaptive mesh refinement hierarchy. For more details we refer the reader to the aforementioned code description papers as well as the online documentation.

Gas Treatment For the data given here AHF version v1.0-021 was run in two configurations: one where the thermal energy of the gas entered the unbinding procedure via

$$e_{\text{gas}} = \phi + \frac{1}{2}v^2 + u \quad (1)$$

where e_{gas} is the total specific energy (required to be negative for bound particles), ϕ the gravitational potential, v the gas particle's velocity and $u = \frac{3}{2} \frac{k_B}{m} T$ its thermal energy, and a second one where this feature was switched off (i.e. $u = 0$).

3.2 JUMP-D (Casado & Dominguez-Tenreiro)

JUMP-D is a galaxy finder and *not* a sub-*halo* finder and hence is treated differently than the other finders in this work. It aims at finding and measuring central and satellite galaxies within given host haloes, i.e. *baryonic* substructure objects within a sphere of given radius R_{lim} about the centre of the host. To this extent the stellar and gas mass profiles are searched for jumps (and hence the name) in the three-dimensional cumulative mass profiles from the host halo centre out to the limiting radius R_{lim} (i.e. usually the host halo's virial radius). The jump detection criterion is based on the detection of changes in the first and second derivatives of the respective mass profiles in the r , θ and ϕ variables at the substructure locations corresponding to the humps they cause. For the stellar object, the jump in the stellar mass profile is used as a first satellite detection (i.e., location and velocity), that is later on refined by searching for maxima in 6-dimensional phase-space within an allowance region about that first center, returning the object stellar sizes r_{star} as well. The jumps in the gas profile are then matched to the stellar objects and gas particles inside a spherical region defined by the radial extend of the gas jump (r_{gas}) are then associated to the stellar object. Note that for the detection of the jumps only cold gas is considered.

Please note that the approach of JUMP-D is substantially different to halo finders in general. The code *only* locates a baryonic object ("galaxy") without considering the dark matter. To this extent JUMP-D cannot be subjected to the common post-processing pipeline (cf. Section 3.6) when it comes to subhaloes as that pipeline heavily relies on the embedding of satellite galaxies within dark matter subhaloes. Therefore, JUMP-D only contributes to those plots where the identities of such dark matter subhalo particles is not required. The situation is different for field/host haloes where it is more straight forward to identify the surrounding dark matter halo and its virial radius. In that regards, JUMP-D has been passed through the pipeline for the results presented in Section 4.

Gas Treatment For the satellite galaxies we take advantage of the bi-phase nature of the gas in this particular simulation, and just consider the cold gas when detecting jumps in the gas profile. To determine the cut in internal energy separating both the cold and hot gas regimes, the thermal energy distribution of gas particles within

² AHF is freely available from <http://www.popia.ft.uam.es/AHF>

the host virial radii is studied and its minimum is used to separate the two phases and reject the hot gas from the object, respectively. However, this is only applied to the satellite galaxies and not the three main objects where all gas irrespective of its phase is added.

3.3 ROCKSTAR (Behroozi)

ROCKSTAR (Robust Overdensity Calculation using K-Space Topologically Adaptive Refinement) is a phase-space halo finder designed to maximise halo consistency across timesteps (Behroozi et al. 2011). The algorithm first selects particle groups with a 3D Friends-of-Friends (FOF) variant with a very large linking length ($b = 0.28$). For each main FOF group, Rockstar builds a hierarchy of FOF subgroups in phase-space by progressively and adaptively reducing the linking length, so that a tunable fraction (70 per cent, for this analysis) of the particles are captured within each subgroup as compared to the immediate parent group. When this is complete, Rockstar converts FOF subgroups into seed haloes beginning at the deepest level of the hierarchy. If a particular group has multiple subgroups, then particles are assigned to the subgroup seed haloes based on their phase-space proximity. This process is repeated at all levels of the hierarchy until all particles in the base FOF group have been assigned to haloes. Unbinding is performed using the full particle potentials; halo centres and velocities are calculated in a small region close to the phase-space density maximum. Rockstar is a massively parallel code (hybrid OpenMP/MPI style).

Gas Treatment As already mentioned, initially ROCKSTAR provided a particle ID list that was based upon an analysis that treated each particle equally (without even taking into account the difference in mass between the phases). In the common post-processing stage (see Section 3.6 below for more details) an unbinding procedure was then applied outside of ROCKSTAR. However, this unbinding (deliberately) did not take into account the thermal energy of the gas, but only considered the kinetic and potential energy of all the particles.

3.4 STF (Elahi)

The STructure Finder is a parallel hybrid OpenMP/MPI code (Elahi et al. 2011, STF) that identifies objects by utilizing the fact that dynamically distinct substructures in a halo will have a *local* velocity distribution that differs significantly from the mean, *i.e.* smooth background halo. This method consists of two main steps, identifying particles that appear dynamically distinct and linking this outlier population using a Friends-of-Friends-like approach. Since this approach is capable of not only finding subhaloes, but tidal streams surrounding subhaloes as well as tidal streams from completely disrupted subhaloes, for this analysis we also ensure that a group is self-bound. Particles which are gravitationally unbound to a candidate subhalo are discarded until a fully self-bound object is obtained or the object consists of fewer than 20 particles, at which point the group is removed.

Gas Treatment For this study, we treat each particle type separately, first identifying dark matter (sub)haloes. Gas and star particles are then associated with the closest dark matter particle in phase-space belonging to a (sub)halo. Further, in order to highlight differences in how particles can be treated, we *do not* pass baryonic particles through an unbinding routine. Part of the motivation

for this comes from observational studies. It is quite difficult to determine from observations alone whether gas or stellar structures are bound to a galaxy. Instead, spatially coincident gas and stellar structures lying within the same line-of-sight velocity window are generally assumed to be dynamically related. Hence in this spirit, we do not attempt to determine whether a gas or star particle is bound to a dark matter (sub)halo, nor do we attempt to account for the thermal properties of the gas.

We note that multiple masses do not effect the local velocity distribution function estimate though they do affect the background velocity distribution estimate, specifically the centre-of-mass of the coarse grain cells used to estimate the local velocity distribution.

3.5 SUBFIND (Dolag & Springel)

SUBFIND identifies substructures as locally overdense, gravitationally bound groups of particles. Starting with a halo identified through the Friends-of-Friends algorithm, a local density is estimated for each particle with adaptive kernel estimation using a prescribed number of smoothing neighbours. Starting from isolated density peaks, additional particles are added in sequence of decreasing density. Whenever a saddle point in the global density field is reached that connects two disjoint overdense regions, the smaller structure is treated as a substructure candidate, followed by merging the two regions. All substructure candidates are subjected to an iterative unbinding procedure with a tree-based calculation of the potential. The SUBFIND algorithm is discussed in full in Springel et al. (2001) and its extension to dissipative hydrodynamical simulations that include star formation in Dolag et al. (2009).

Gas Treatment Within SUBFIND the total density at the position of each particle is estimated by summing up the contribution of all the different particle species. In contrast to applying the SPH formalism to all particles at the same time, this allows a much more fine structured density field to be obtained if the particles of the different species have significantly different spatial distributions, as is usually the case for star particles. We use all the particles initially belonging to the substructure candidate in order to evaluate the gravitational potential. For gas particles, we also take the internal thermal energy into account in the gravitational unbinding procedure. If the number of bound particles left is larger than 20 and the object contains at least one star or one dark matter particle, we register the substructure as genuine sub-halo.

3.6 Common Post-Processing Pipeline

As was the case for the previous comparison projects we again subjected all halo finder (except for JUMP-D satellite galaxies) results to a common post-processing pipeline. Code representatives were simply asked to return the particle IDs of those particles they considered to belong to a given object (may that be a host or sub-halo). To this extent, halo positions are iteratively determined centre-of-masses using the innermost 5 per cent of particles (limiting the positional shift per iteration to the force resolution of the simulation, *i.e.* $0.15h^{-1}$ kpc), the bulk velocity is the mean velocity of all particles, the mass corresponds to M_{200} (*i.e.* the mass enclosed in a sphere so that the mean density inside the sphere equals 200 times the critical density of the Universe), and V_{\max} is the peak value of the circular velocity curve. This approach entails that any scatter reported here will be a lower limit as all halo properties are

Table 1. Some general properties of the three main galaxies. Masses are measured in $10^{11} h^{-1} M_{\odot}$, velocities in km/sec, magnitudes are the Johnson V-band magnitude, and the baryon fractions are given as $f_X = M_X / M_{\text{tot}}$ where f_X can be either f_g (gas mass fraction) or f_s (stellar mass fraction). Note that the total baryon fraction is the sum $f_b = f_g + f_s$.

code	Mass			V_{max}			Johnson M_V			gas mass fraction f_g			stellar mass fraction f_s		
	MW	M31	M33	MW	M31	M33	MW	M31	M33	MW	M31	M33	MW	M31	M33
AHF	3.4	4.3	1.7	124	125	119	-20.3	-21.0	-19.5	0.043	0.078	0.066	0.035	0.033	0.037
JUMP-D	3.4	4.2	1.7	124	125	118	-20.3	-20.9	-19.5	0.043	0.077	0.066	0.035	0.034	0.037
ROCKSTAR	3.4	4.3	1.7	124	125	119	-20.3	-21.0	-19.5	0.043	0.078	0.066	0.035	0.033	0.037
STF	3.1	3.3	1.6	124	121	119	-20.3	-20.6	-19.5	0.043	0.079	0.067	0.036	0.032	0.037
SUBFIND	3.2	3.5	1.6	124	123	119	-20.2	-20.6	-19.5	0.042	0.069	0.058	0.035	0.031	0.037

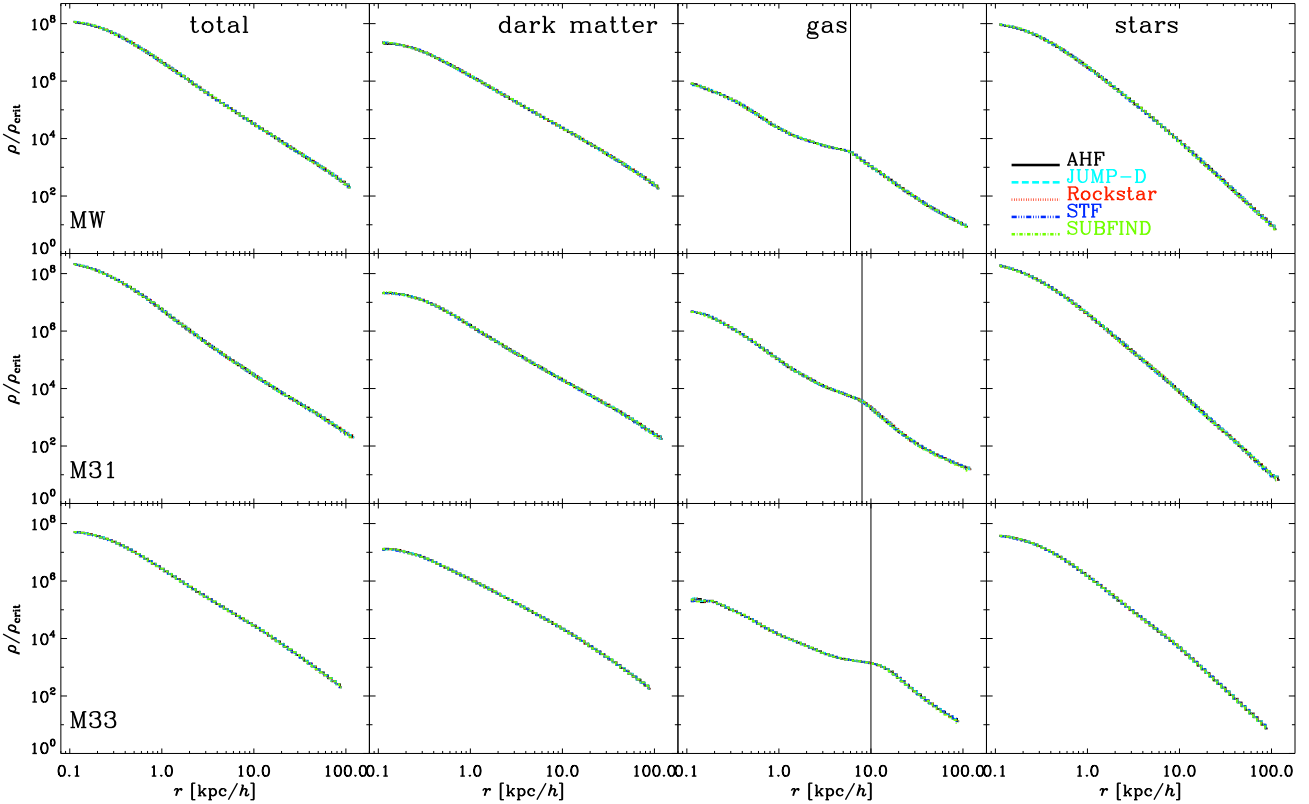


Figure 2. Density profile of the total (first column), dark (second column), gas (third column), and stellar (fourth column) matter for M31 (upper row), the MW (middle row), and M33 (bottom row). The vertical line (coinciding with the ‘kink’ in the gas profile at 8, 6, and $10 h^{-1}$ kpc, respectively, indicates the transition from the central baryon dominated region to the halo and will be used for the bulge-disk decomposition in Section 4.3.

defined in an identical manner. The star particles and their metallicities and ages are used to calculate the luminosities and magnitudes (cf. Section 2.2 for the model). Note that we primarily use magnitude throughout this work, liberally referring to it as “luminosity” in places.

We also need to mention that the mode of operation of this pipeline biases results towards galaxies residing in dark matter haloes: both the definition of the object’s edge and the fact that we require V_{max} to be calculated relies on the fact that the bound dark matter particles within such a subhalo have been identified. Therefore – as mentioned before – the JUMP-D satellite outputs are not best suited to be passed through this pipeline.

4 GALAXY COMPARISON

The present work would not rightfully be called a “Galaxy Comparison Project” if we were not to study the properties of the (baryonic component of the) dominant galaxies in our constrained Local Group simulation, i.e. the MW, M31, and M33. We therefore begin by comparing the particulars of these objects.

4.1 General Properties

In Table 1 we provide a summary of the most fundamental properties of the three main galaxies in our simulation, i.e. we list the mass, V_{max} , luminosity (as characterised by the Johnson V-band

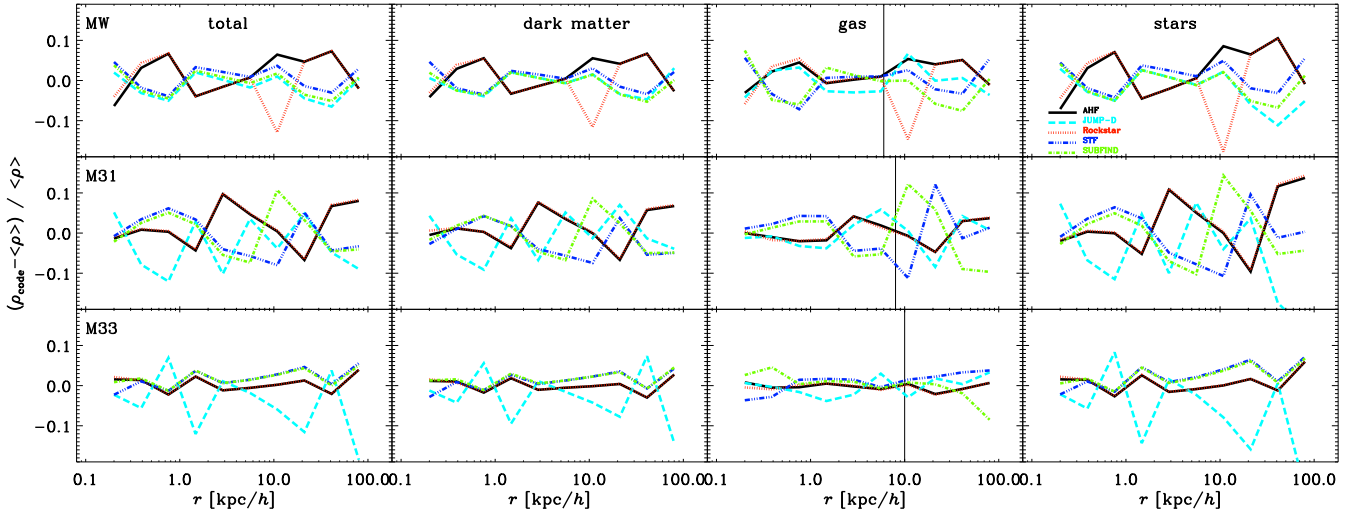


Figure 3. Same as Fig. 2 but this time showing the relative difference to the mean of all density profiles.

magnitude), and baryon fractions $f_X = M_X/M_{\text{tot}}$ where f_X can be either f_g (gas mass fraction) or f_s (stellar mass fraction). Note that the total baryon fraction is the sum $f_b = f_g + f_s$. There is a rather excellent agreement across the halo finders, with the scatter in basically any quantity being smaller than 10 per cent, which was the deviation found in our previous dark matter only comparisons. The remaining differences seen in the mass are readily explained by the fact that some codes (e.g. AHF) consider subhaloes to contribute to the mass of their respective host while others (e.g. STF and SUBFIND) exclude the subhalo masses.

4.2 Mass Distributions

To explore any differences in more detail we now decompose the mass profiles of the three galaxies. The result is presented in Fig. 2 where we show the total matter density profile (left column) and its breakdown into the various components, i.e. dark matter (2nd column), gas (3rd column), and stars (rightmost column). The rows represent the MW (upper row), M31 (middle row), and M33 (bottom row).

All finders agree outstandingly well for all three components (and hence the total matter, too). Despite their different treatment of the gas thermal energy, the resulting mass distributions throughout the three galaxies remain essentially indistinguishable. When comparing the profiles to the numbers in Table 1 one may wonder about M31 and why it is that while the masses differ by 30 per cent the density profiles agree so remarkably well. This is readily explained by differences in the virial radii of approximately 10 per cent, something not clearly visible in Fig. 2 due to the logarithmic x -axis. In that regard, note that all the curves in the figure terminate at the respective virial radius and go slightly closer to the centre than the nominal force resolution of the simulation, i.e. $0.15h^{-1}$ kpc. These variations in mass and radius are partly due to different treatment of subhalo masses: some codes include substructure in the host mass (e.g. AHF) whereas other do not (e.g. SUBFIND). And this is particularly important for the simulated M31 as it contains one large group of satellites contributing approx. 15 per cent of the total host mass (cf. Sec. 4.2.1 in Klimontowski et al. 2010, where this particular object is discussed in detail). However, the mass and radii differences are also affected by

disparate particle collection and unbinding procedures (Knebe et al., in preparation) accounting for the remaining variations across codes.

Another interesting aspect of Fig. 2 is the kink in the gas density profile apparent at approximately $6\text{--}10h^{-1}$ kpc, corresponding to roughly 10 per cent of the virial radius (with no difference across finders again). This peak represents the transition from the central baryon dominated region to the halo and will be used in the following Sub-Section for the bulge-disk decomposition.

To better gauge the differences across finders we additionally plot in Fig. 3 the fractional differences between the profile of each finder and the respective mean profile when averaging over all codes. This figure shows that the residual scatter of the density profiles is at most just 10 per cent about the mean.

4.3 Dynamical Bulge–Disk Decomposition

A dynamical bulge–disk decomposition for all three central galaxies in our simulation has been performed. We decompose the galaxies using two different techniques, one for the gas and one for the stars.

For the star particles we apply the method proposed by Abadi et al. (2003), used by Okamoto et al. (2005), and improved upon in Doménech-Moral et al. (2012). The method is to essentially compare the z -component of the angular momentum (J_z) of each particle with the angular momentum of a circular orbit with the same energy, $J_c(E)$. The first step is to thus define a z -direction which, as suggested by Abadi et al. (2003) may be chosen to be the total (specific) angular momentum of all the star particles inside the “luminous radius” of the galaxy (defined here as within 6, 8, and $10h^{-1}$ kpc for the MW, M31, and M33, respectively; see the kink in the gas profiles visible in Fig. 2). The choice of a z -direction in this manner ensures that the majority of the particles will have positive values of J_z . The potential and kinetic energy for each star and gas particle within this luminous radius of the galaxy is then calculated. Since circular orbits maximise angular momentum, we assume $J_c(E)$ for a particle of energy E is simply the maximum value of J_z of all particles with that energy. Note that the limits of $\epsilon = J_z/J_c(E)$, i.e. -1 and 1, correspond to counter- and co-rotating particles on circular orbits. Spheroidal systems with very little net

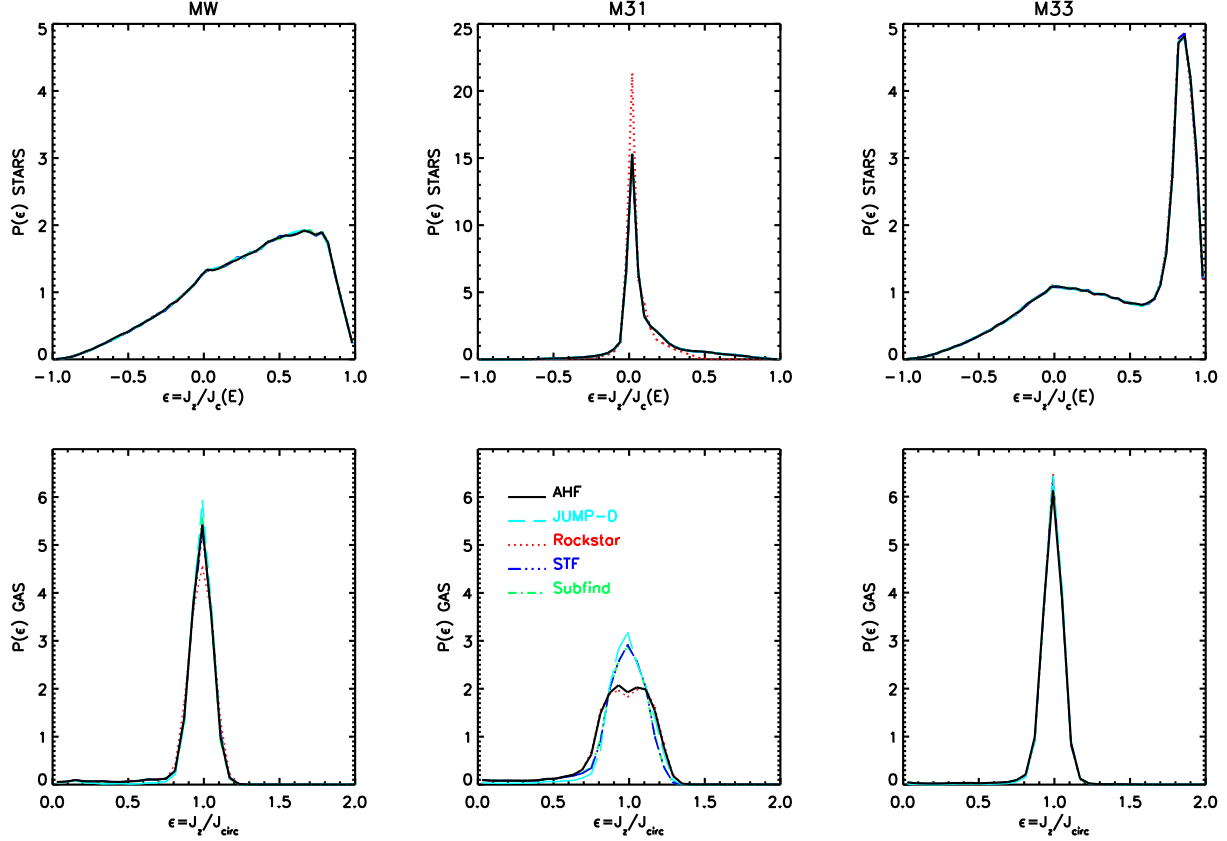


Figure 4. A dynamical bulge - disc decomposition for stars (top) and gas (bottom) particles in the MW (left), M31 (middle) and M33 (right). We compare each star particle's angular momentum in the z -direction to the angular momentum of a circular orbit of the same energy and show on the y -axis the probability density distribution $P(\epsilon)$, for a given $\epsilon = J_z/J_c(E)$. For gas particles we compare the angular momentum in the z -direction with the angular momentum of a circular orbit at that radius and show on the y -axis the probability density distribution $P(\epsilon)$, for a given $\epsilon = J_z/J_{\text{circ}}$.

rotation are thus represented by a Gaussian centred on 0. A fully rotationally supported thin disc on the other hand is represented by values of $J_z/J_c(E) \approx 1$. Thick disks not fully supported by their rotation can be seen as distributions centred on positive values such as $J_z/J_c(E) \approx 0.5$ (Abadi et al. 2003).

The resulting distributions can be viewed in the upper panels of Fig. 4. All three galaxies contain both co- and counter rotating populations. The MW comprises a bulge and a (co-rotating) thick disk that peaks at $\epsilon \approx 0.8$. No thin disc is seen here, although owing to their relatively high values of ϵ , many particles in the thick disc are kinematically cold. M31 on the other hand appears as a featureless spheroid whose net angular momentum can be seen as a fat tail towards positive values of ϵ . M33 is a more model galaxy - it contains a well defined rotationally supported thin disc as well as a central bulge and a small, kinematically hotter, thick disc component.

While all this is certainly interesting in terms of galaxy formation, the most important part to note – with respect to this comparison project – is that all halo finders behave similarly when examining this stellar decomposition.

For the decomposition of the gas particles we use a slightly different method because some of the halo finders include the internal energy in their unbinding procedure, while others do not. Unlike the stars, it is thus unfair to decompose the gas distribution on energetic grounds. Consider a co-rotating stellar and gaseous disc. Some halo finders will use the internal energy of gas particles to un-

bind them from this coherent motion and thus exclude them from the dynamical decomposition described above. In this case, while all halo finders will easily pick out star particles that are on circular orbits, not all gas particles on circular orbits will be included. The results of such a dynamical decomposition comparison are thus unreliable.

In order to overcome this inconsistency we use a method proposed by Scannapieco et al. (2010). As with the stars, a z -direction is defined to be the total angular momentum of all gas particles within 6, 8, and $10h^{-1}$ kpc for the MW, M31, and M33, respectively. We then calculate the ratio of $\epsilon = J_z/J_{\text{circ}}$ where J_{circ} is the angular momentum of a circular orbit at the same radius, i.e.

$J_{\text{circ}} = r \times \sqrt{\frac{GM(<r)}{r}}$. In this way we bypass the need to use the potential and kinetic energies since, as mentioned earlier, gas particles also have thermal energies. When this ratio is equal to unity, a gas particle is moving on a circular orbit (with respect to the z -direction). Note that this ratio is in principle unbounded from $(-\infty, \infty)$. In practice however, few (~ 1 per cent gas particles counter rotate and thus a lower limit of zero is applicable).

The decomposition of the gas particles is shown in the bottom panels of Fig. 4. All gas distributions exhibit peaks at $\epsilon = 1$, indicating the presence of gaseous discs. M31 has a wider distribution implying a thicker, dynamically hotter component (as also suggested by the stellar decomposition above it). It is interesting to note that in M31 AHF and ROCKSTAR identify a small local minimum around $\epsilon = 1$. This dip (with different maxima to the left

Table 2. Number of subhaloes (compliant with our selection criterion, see text for details) found by each participating halo finder. For JUMP-D we list the number of baryonic objects found.

code	N_{sub}^{MW}	N_{sub}^{M31}	$N_{\text{sub}}^{\text{combined}}$
AHF	32	43	75
JUMP-D	25	35	60
ROCKSTAR	29	38	67
STF	31	42	73
SUBFIND	31	40	71

and the right) is interpreted as a subtle warping of the gaseous disc. The astute observer will also notice a small but non-negligible tail towards zero in the MW and M31 distributions; these are gas particles whose angular momentum in the z -direction is smaller than that of a circular orbit of this radius and who are thus on either radial or inclined orbits.

The minor discrepancies between halo finders for the gas component are certainly due to the differences in the handling of gas particles: for instance, AHF as well as SUBFIND read the gas thermal energy taking it into account during the unbinding procedure; all other codes do not consider the thermal energy at that stage (STF and ROCKSTAR) or do not feature an unbinding procedure (JUMP-D).

5 SATELLITE COMPARISON

We now turn to taking a closer look at the satellite populations of the two prominent host haloes, i.e. all subsequent plots are based upon a combined sample of MW and M31 subhaloes that reside inside a sphere of radius 300 kpc centred on their respective host *and* that contain at least one star particle. Note that this radius is slightly larger than the virial radii of the two hosts (≈ 200 kpc) and motivated by the observationally inferred value (Watkins et al. 2010). We further impose a lower limit for $V_{\text{max}} \geq 10$ km/sec as this corresponds to the completeness level (cf. Fig. 5 below). We list in Table 2 the number of subhaloes compliant with these criteria found by each of the participating finders.; and for JUMP-D we give the number of baryonic objects found. Further note that JUMP-D is in the special situation of not considering subhalo finding and hence is not suited to be subjected to the common post-processing pipeline. Therefore, JUMP-D only contributes to the plots that merely require knowledge of the baryonic component. This data has been directly provided by the finder itself.

5.1 V_{max} Function

We start with a quantity that has caught a lot of attention recently, especially for the Local Group/Milky Way dwarf spheroidal galaxies (dSph's): the peak of the circular velocity curve V_{max} (e.g. Boylan-Kolchin et al. 2011b; di Cintio et al. 2011; Boylan-Kolchin et al. 2011a; Vera-Ciro et al. 2012; Di Cintio et al. 2012). It has, for instance, been shown by di Cintio et al. (2011) that the inclusion of baryonic physics into the simulation can lead to variations in V_{max} (and R_{max}) when being compared to dark matter only simulations; in particular, (sub-)haloes with high baryon fractions tend to experience adiabatic contraction while objects with lower baryon content move towards lower- V_{max} /higher- R_{max} values, possibly

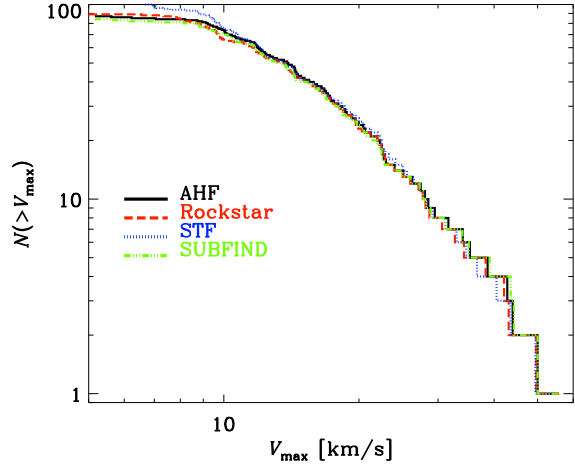


Figure 5. Cumulative V_{max} function for haloes closer than 300 kpc to either of the two simulated hosts M31 and MW that at least contain one star particle.

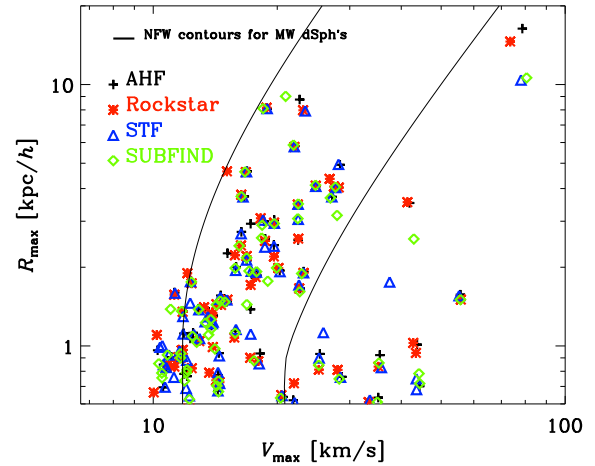


Figure 6. The relation between the peak of the circular velocity curve V_{max} and its position R_{max} for subhaloes inside a 300 kpc sphere about either M31 or the MW. The thin solid lines delineate the 1σ confidence interval of the observed bright MW dSph galaxies (as in Boylan-Kolchin et al. 2011b; di Cintio et al. 2011).

due to mass outflows (Navarro et al. 1996) or random bulk motion of gas “heating” the central matter distribution (Mashchenko et al. 2006).

In Fig. 5 we compare the cumulative distribution of V_{max} found by all our finders. We find excellent agreement. Please note that this is the only plot that has not been subjected to the lower V_{max} limit.

5.2 $R_{\text{max}} - V_{\text{max}}$ relation

As already outlined above when motivating the consideration of the V_{max} function in the first place, there has been some substantial debate about the failure of the most massive subhaloes found in simulations of Milky Way type dark matter host haloes to host the most luminous observed dSph's (Boylan-Kolchin et al. 2011b; di

Cintio et al. 2011; Boylan-Kolchin et al. 2011a; Vera-Ciro et al. 2012; Di Cintio et al. 2012). To verify whether different halo finders will contribute differently to this discussion we present in Fig. 6 the usual plot confronting R_{\max} with V_{\max} . The two solid lines delimit the 1σ confidence interval of the observed bright Milky Way dwarf spheroidal galaxies, as defined in Boylan-Kolchin et al. (2011b); di Cintio et al. (2011, please refer to these references for more details).

We again find remarkable agreement across the participating codes, even though there appears to be some marginal scatter across R_{\max} values. This can be attributed to the fact that the determination of V_{\max} is certainly more stable for cosmological dark matter haloes due to the flatness of the circular velocity curve; and this flatness is obviously also responsible for (slight) variations in the position of the peak velocity. In that regard, it should be noted that in order to best calculate the position of the peak, i.e. R_{\max} , in the circular velocity curve we decided to only use the dark matter for this purpose, i.e. R_{\max} is defined as the position of the maximum of $M_{\text{DM}}(< r)/r$; however, $V_{\max}^2 = GM_{\text{tot}}(< R_{\max})/R_{\max}$ obviously takes into account all matter.

5.3 Baryonic Mass

In Fig. 7 we show the cumulative stellar (top) and gas mass (bottom) function of all our subhaloes. The number of objects in the stellar mass plot corresponds to the one given in Table 2. But we also acknowledge that this number is smaller than the total number of "subhaloes with stars" found by the majority of finders as can be seen in Fig. 5 due to the now applied V_{\max} cut.

While the stellar masses of the objects agree remarkably well (note that JUMP-D returns the stellar masses of the objects within r_{star} , and hence their slightly smaller values in some cases), we notice quite substantial differences in the gas masses. While we return to the differences found for the gas fractions in subhaloes in more detail later, we bear in mind that the actual number of subhaloes containing any gas is rather low for the majority of finders (note that JUMP-D returns the cold gas masses within r_{gas} only when cold gas exist at the satellite center). STF, which does not perform an unbinding procedure for the gas, finds a substantial number of satellites containing gas particles down to the limit of one gas particle. The mass of a gas particle is $m_{\text{gas}} = 4.4 \times 10^4 h^{-1} M_{\odot}$ which corresponds to the lower limit of the x -axis.

While the agreement of the (stellar) masses appears to indicate that the objects found by the suite of finders used here are the same, this is not necessarily the case given their different modi of operations. To shed some more light on the cross-correlation of objects (in a statistical sense) we follow Onions et al. (2012) and plot in Fig. 8 the cumulative stellar mass in objects as a function of distance from the centre of the host halo (normalized to the host radius). We stack the data from the MW and M31. The agreement proves that the satellite galaxies not only have similar masses but also live at approximately the same distance from the central galaxy. There are, however, a few (massive) objects found by JUMP-D and STF close to the centre not picked up by the other finders. There is another interesting feature in this plot, namely that JUMP-D is slightly below the other finders at larger radius, which is possibly due to ignoring the underlying dark matter, so that either the individual galaxies have less stars or some with a low stellar content are missed because without the dark matter particles they are too small to be assigned as reliable substructures.

So far we have separated stellar and gas mass when studying baryons. But we now briefly turn to the baryon fraction, investigating its relation with V_{\max} in Fig. 9. Again, all codes show the same

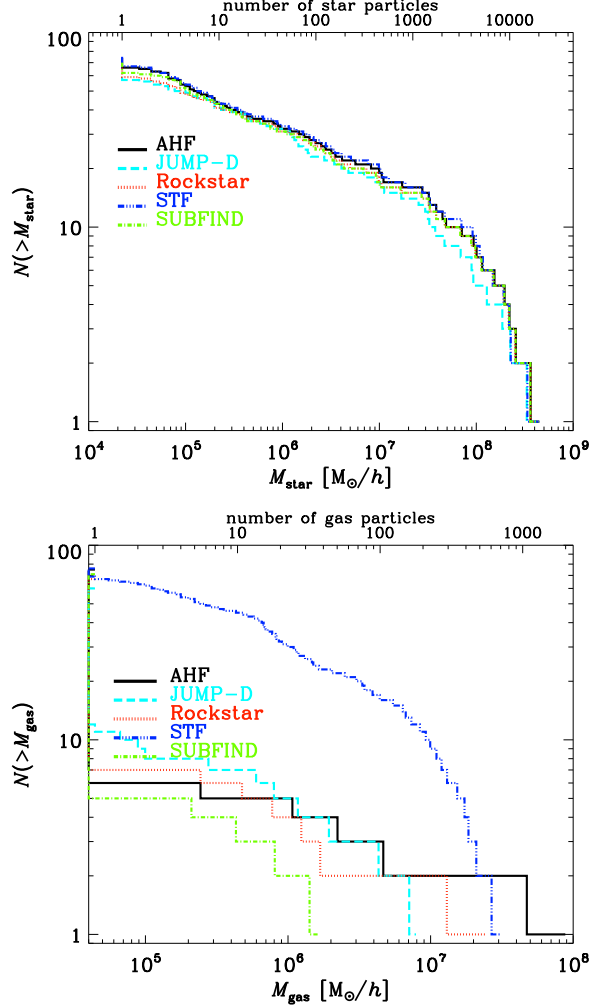


Figure 7. Cumulative stellar (top) and gas (bottom) mass functions for the same objects already shown in Fig. 6. The upper x -axis of each panel provides a translation of mass into number of particles.

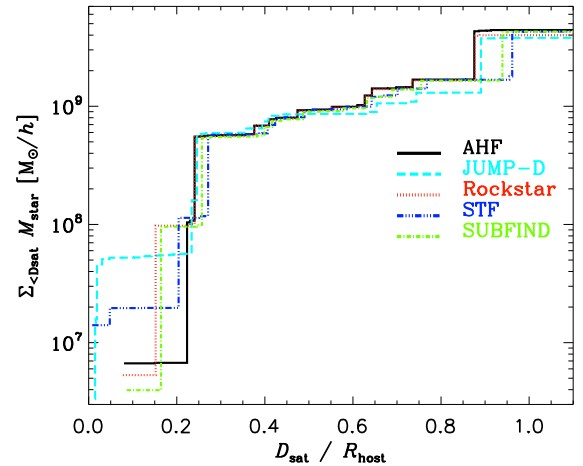


Figure 8. Cumulative stellar mass in objects as a function of distance to the (normalized) host centre.

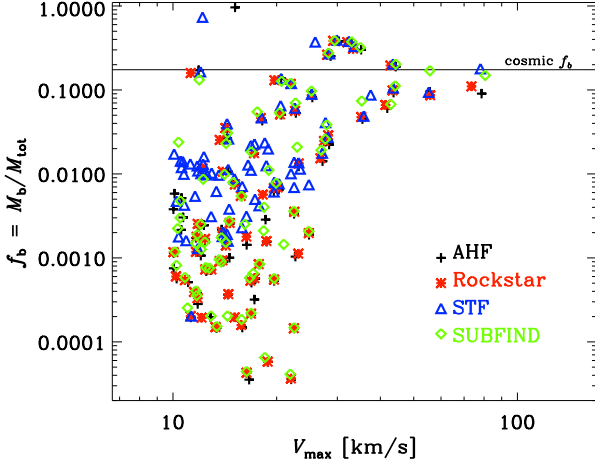


Figure 9. Baryon fraction f_b vs. V_{\max} .

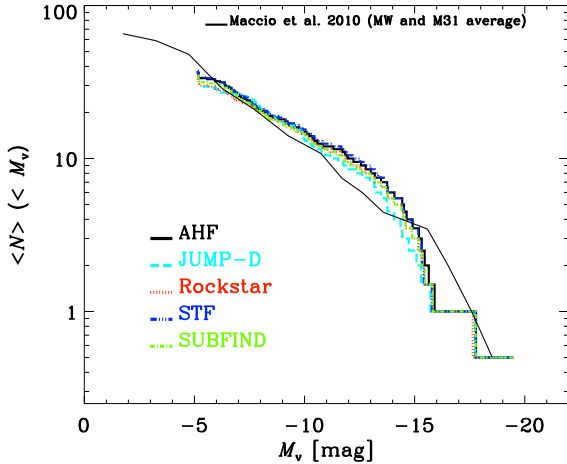


Figure 10. The luminosity function of subhaloes in the Johnson V-Band. The “Maccio” observational data (thin solid line) is a combination of the volume corrected MW luminosity function Koposov et al. (2008) augmented with information from Mateo (1998) and Macciò et al. (2010) under the assumption of an NFW-like radial distributions of satellites. Note that the comparison to the observational data is *not* the prime target of this study and only serves as a reference.

tendency for more massive subhaloes to also contain more baryons and it is difficult to decipher any differences (despite our knowledge that there are marked differences in the gas content), unless we move to a comparison of objects on a one-to-one basis to be undertaken in Section 6. However, we note that STF does not find as many low- f_b objects (for $V_{\max} < 20$ km/sec) as the other finders due to the fact that it keeps more gas in its subhaloes as seen in (the bottom panel of) Fig. 7. Bear in mind again that STF did not pass the gas particles through an unbinding routine, hence the expected large gas fractions at all mass scales.

5.4 Luminosity Function

In Fig. 10 we now present the Johnson V-Band luminosity function as well as the observational data as taken from Koposov et al.

(2008) and Macciò et al. (2010), respectively (thin solid line, referred to as “Maccio sample”): these data are a combination of the volume corrected MW satellite luminosity function (Koposov et al. 2008) augmented with information from Mateo (1998) and Macciò et al. (2010) kindly provided to us by Andrea Macciò (personal communication). And even though all luminosity functions agree with the Maccio sample rather well, we stress that we included the observational data merely as a reference to guide the eye. It is not our prime objective to reproduce the MW and/or M31 luminosity function of satellite galaxies with our simulation. We find again excellent agreement between the finders. But this comes at no surprise as we found negligible variations in the stellar mass of subhaloes in (the upper panel of) Fig. 7 already.

6 SATELLITE CROSS-COMPARISON

While the general agreement for the satellite populations between codes is rather outstanding – at least when it comes to the fundamental characteristics such as V_{\max} and luminosity M_V – we now go one step further and directly compare properties of objects on an individual basis. To this extent we use the same matching criterion (based upon the uniqueness of particle IDs) successfully used to construct merger trees or cross-correlate different simulations before (e.g. Klimentowski et al. 2010; Libeskind et al. 2010; Knebe et al. 2011) by facilitating a tool that comes with the AHF package called *MergerTree*. Even though originally designed to identify corresponding objects in the same simulation at different redshifts it can equally be applied to find “sister objects” in an analysis of the same snapshot done with a different halo finder.

Note that distribution functions (as well as scatter plots) previously presented will not only suffer from differences in individual halo properties but also encode the fact that some finders may have identified different numbers of objects (cf. Table 2). To circumvent this we aim at directly comparing quantities on a halo-to-halo basis and move from general distribution functions and their variations as discussed above to cross-comparing satellites. The plots in the following Sub-Sections 6.2 through to 6.4 now all follow the same logic: the x -axis shows the median of the haloes’ V_{\max} , whereas the y -axis gives the normalised difference between the lower and upper percentiles equivalent to the 2nd and 3rd ranked of the distribution across all halo finders (JUMP-D is not included in these plots as no dark matter halo required for the calculation of V_{\max} has been provided). We deliberately chose to use medians and percentiles as the distribution of properties across finders might be non-Gaussian and at times biased by just one outlier. Further note that not all subhaloes have an error greater than zero: those for which the difference in the 3rd and 2nd ranked finder is zero have been artificially placed at the bottom of each panel at a value of 1.2×10^{-4} yet entered with their correct value of zero into the calculation of the error percentages given below in the respective Sub-Section. We further indicate the 1 per cent and 10 per cent error by a horizontal dashed line in each plot and provide the fraction of those objects below that error as a legend.

6.1 A Common Set

For a given subhalo in one catalogue we locate the subhalo which contains both the greatest fraction of its particles and which is closest to it in mass. Specifically, for each sister candidate i we calculate a merit m_i , defined as

$$m_i = \frac{n_{\text{shared},i}^2}{n_{\text{reference}} n_{\text{sister},i}} \quad (2)$$

where $n_{\text{shared},i}$ is the number of particles shared between both subhaloes, $n_{\text{sister},i}$ is the total number of particles in the sister candidate and $n_{\text{reference}}$ is the total number of particles in the reference subhalo. We then identify the sister as that halo with the largest value of m_i . Typically, successful matches result in $m_i \gtrsim 0.5$ and we assume to have failed to find a sister if $m_i < 0.2$ for a given subhalo.³

By restricting ourselves to the set of objects found by *every* halo finder we are able to directly compare the properties of *the same object* across all finders. Even though AHF found the most haloes compliant with our initial selection criterion and we chose to use its catalogue as the basis, we confirm that every subhalo found by AHF has an actual counterpart in all other analyses. However, some of these counterparts do not fully lie within the required 300 kpc-sphere and hence were rejected from the previous analysis. Using them now will increase our statistics without obscuring the results: the aim is to compare the same objects across different finders and they certainly serve this purpose.

6.2 V_{max} & R_{max}

While we have seen that the general relation between the codes for subhaloes compliant with our selection criterion is rather remarkable, Fig. 11 further confirms that also the one-to-one scatter of cross-identified objects is small: inspecting the differences in the peak of the circular velocity curve V_{max} and its location R_{max} , we find the overall median values of the error to be < 1 per cent and 2 per cent for V_{max} and R_{max} , respectively. It is evident that V_{max} gives better agreement as it is a more stable property than R_{max} due to the flatness of the circular velocity which is responsible for at least a part of the scatter in R_{max} .

6.3 Baryons

The comparison of the gas mass function in Fig. 7 already revealed differences while the stellar mass function showed excellent agreement. It therefore comes as no surprise that we find a median error of 86 per cent for the gas mass M_{gas} (considering only subhaloes that actually contain gas) and < 1 per cent for the stellar mass M_* in Fig. 12. As already noted, some subhaloes may be missing from the plot if the difference between their 3rd and 2nd ranked finders is zero. This is in fact the case for some of the objects entering the stellar and gas mass comparison: 47 (out of the 75 successfully cross-matched subhaloes) show identical stellar masses and 63 have no gas particles at all. In that regard, the actual median error of the gas mass is 0 per cent (while the stellar mass value remains unaffected), but we decided to rather report the deviation only considering subhaloes containing gas and seen in the plot, respectively.

How does the error in baryons with the simultaneous agreement in stellar mass translate into differences in the baryon fraction of subhaloes? This can be verified in Fig. 13 where we find an

³ We found these criteria to give the most reliable merger trees for subhaloes (e.g. Klimentowski et al. 2010; Libeskind et al. 2011; Knebe et al. 2011; di Cintio et al. 2011; Libeskind et al. 2011; Di Cintio et al. 2012) and hence decided to apply them also for the cross-correlation.

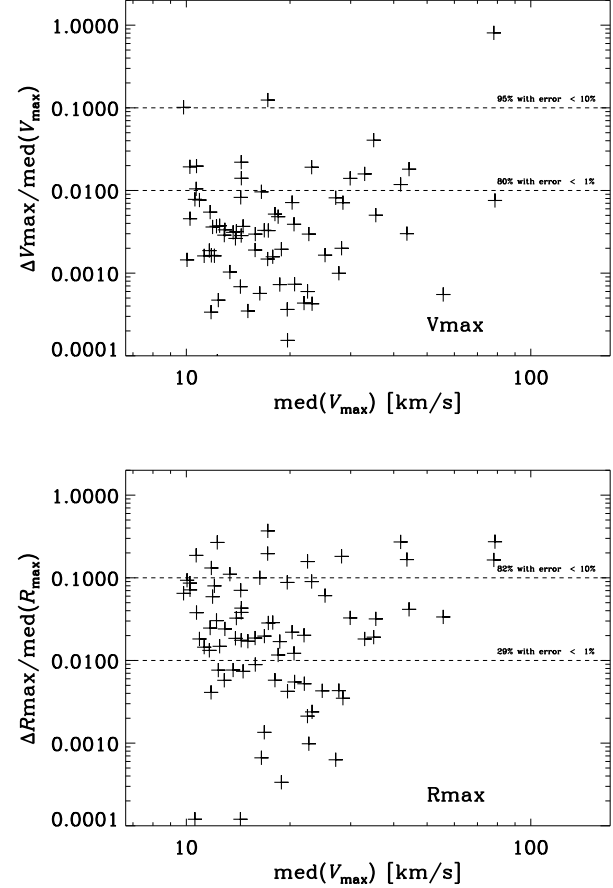


Figure 11. Relative error in V_{max} (top) and R_{max} (bottom). The horizontal dashed line simply indicates an error of 1 per cent for reference. Subhaloes appearing at an error value of 1.2×10^{-4} are the ones that actually have zero values.

overall scatter of 5 per cent. This leads to the conclusion that the stellar mass content is by far the most dominant and important for the baryon fraction and the substantial differences in gas mass only affect its value marginally.

6.4 Luminosity

While the agreement between codes for the V-band magnitude was rather excellent – as verified by the luminosity function presented in Fig. 10 – will we find similar consistency when comparing objects on an individual basis? This can be verified in Fig. 14 where we find a general median error of < 1 per cent (noting again that 47 out of 75 cross-matched subhaloes contain an equal amount of star particles). One thing to note here is that the errors for M_V are a fair bit smaller than the differences found for the stellar masses, even though luminosities are directly related to the star particles (and their properties like age and metallicity). But while the transformation from the upper panel of Fig. 12 to Fig. 14 is most certainly non-linear, the general features (and “satellite placement” in the plot) are nevertheless preserved; the objects are only shifted towards smaller errors entailing that luminosity as measured here via M_V is not as sensitive to the stellar content as the mass itself.

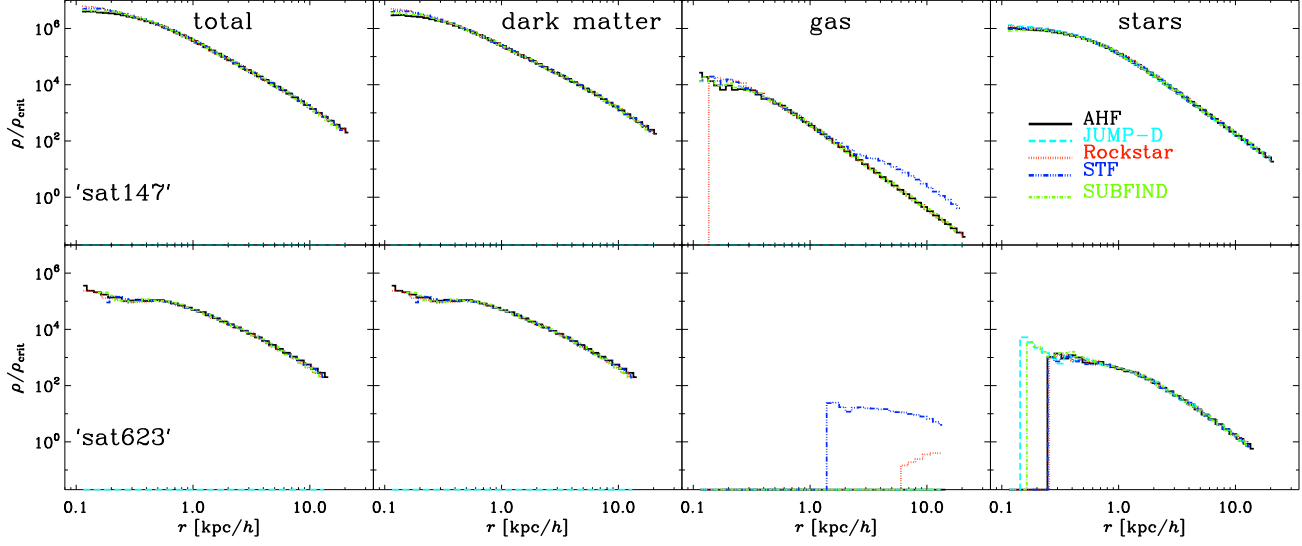


Figure 15. Density profile of the total (first column), dark (second column), gas (third column), and stellar (fourth column) matter for a massive (upper row, called 'sat147') and a low-mass (lower row, called 'sat623') subhalo.

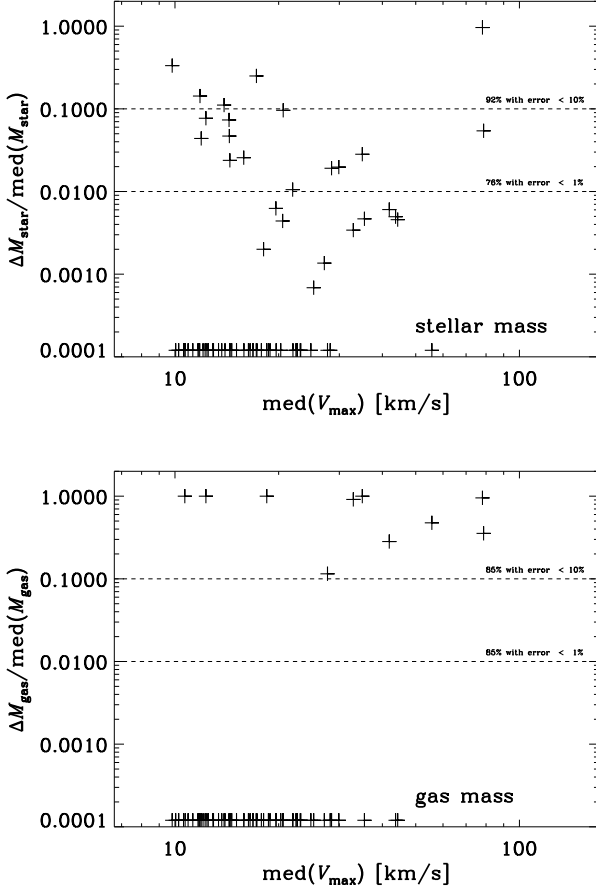


Figure 12. Same as Fig. 11 but for stellar mass M_* (top) and gas mass M_{gas} (bottom).

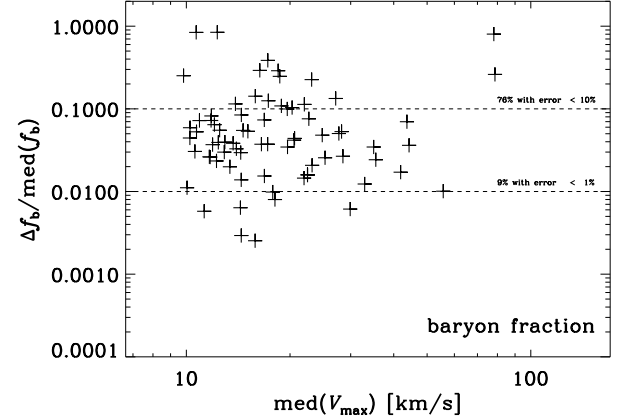


Figure 13. Same as Fig. 11 but for the baryon fraction $f_b = (M_* + M_{\text{gas}}) / M_{\text{tot}}$.

6.5 Mass Distributions

To further explore the differences – in particular for the gas content of subhaloes – we look at the mass distribution of the various components (i.e. dark matter, gas, and stars, as already done for Fig. 2) in the subhaloes found by AHF and cross-matched to all other halo finders. In Fig. 15 we showcase two examples, one massive subhalo (top row, containing roughly 20000 particles) and one less massive object (bottom row, containing 3500 particles); note that using objects with even lower numbers of particles will no longer provide credible profiles. From left to right the columns show the total matter profile, the dark matter, the gas, and the stellar mass profile (all in units of the critical density at redshift $z = 0$). While we can again confirm rather excellent agreement for the dark matter and stars, we clearly see differences in the gas – as expected from the previous plots. In particular, the lower mass subhalo does not feature a gas profile at all for the majority of the applied halo finders. Note again that all curves terminate at the edge of the object.

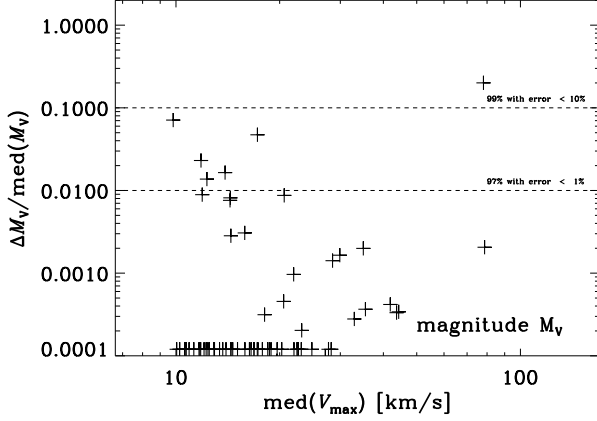


Figure 14. Same as Fig. 11 but for the Johnson V-band magnitude M_V .

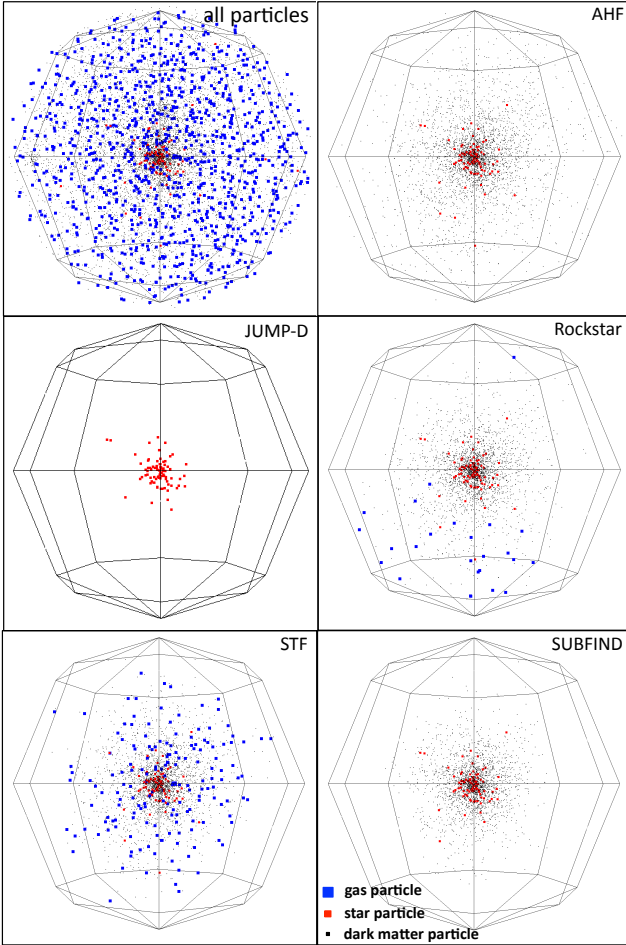


Figure 16. Visualisation of a subhalo showing all particles inside a spherical region about the identified centre (upper left panel) vs. the actually identified particles of the individual halo finder showing all types of particles: gas (blue), stars (red), and dark matter (black). Note that the object coincides with the lower panel object of Fig. 15.

6.6 Gas Treatment – A Test Case

To better understand the differences seen in the gas properties in Figs. 7, 12 as well as 15 we went back to the simulation data and extracted all the particles in a spherical region about the centre of the subhalo featured in the lower panel of Fig. 15. The results can be viewed in Fig. 16. We can clearly see that the region about the object’s centre contains a substantial number of gas particles (shown in the upper left panel). But all codes featuring a treatment of the gas thermal energy either during or prior to the unbinding (i.e. AHF and SUBFIND) remove essentially all gas from the subhalo; the other two finders that do not include the thermal energy during the unbinding are left with a residual amount of gas.

When using AHF in the case where the gas thermal energy has been ignored, AHF basically considers *all* gas particles seen in the left panel to be part of the subhalo. In contrast, due to their phase-/velocity-space nature, both ROCKSTAR and STF consider the majority of the gas particles to belong to the background host and keep only a small amount of them. For the object considered here the effective thermal velocity of each gas particle is always larger than its kinetic velocity (not shown here) and hence the grouping in phase- or velocity-space will naturally remove (hot) gas whenever a gas particle is considered not belonging to it based upon kinetic velocity only. Or put differently, the gas component forming part of the background halo is prone to be removed by such finders as they inherently use velocity information when grouping and collecting the initial set of particles, whereas configuration space finders only deal with velocities (either kinetic or thermal) in a (post-processing) unbinding procedure. On a side note, a visual inspection of a larger region about this particular sample satellite galaxy indicates that it has passed extremely close to its host already and been subjected to severe tidal forces; this might also explain why ROCKSTAR appears to only have found one side of the object.

To verify that in actuality all gas particles should have been removed we finally show in Fig. 17 the same region again (left panel, slightly different projection) alongside the pressure and density of the gas particles along the x -axis (right panel). We can clearly see that the gas particles inside the $5h^{-1}$ kpc sphere about the centre (marked in green) are forming part of the overall background gas particles (marked in blue). The stars (red) are only shown as a reference.

In summary, while configuration space finders such as AHF and SUBFIND require a proper treatment of the gas’ thermal energy to remove (unbound) gas particles belonging to the background, phase-/velocity-space based finders such as ROCKSTAR and STF encode part of this removal into their methodology. However, they keep a residual amount of gas.

7 SUMMARY & CONCLUSIONS

We set out to compare the performance of object finders for cosmological simulations in the case where the data not only contains dark matter but also baryons, i.e. gas and stars. Both types of matter obviously cluster more strongly, gas being able to dissipate its energy, and star particles forming at the bottom of deep potential wells out of the cold gas. While star particles only feel gravity (like the dark matter particles), they nevertheless originated from different sites and more compact regions, respectively. Also gas particles carry a thermal energy acting like a pressure (given an appropriate equation of state). At present, halo finders deal with these subtleties differently, with some properly accounting for the gas pressure and

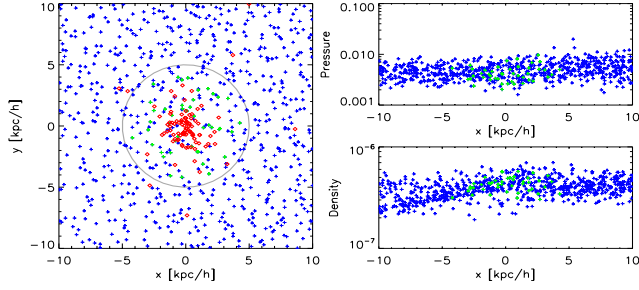


Figure 17. Gas and star particles for the same object as in Fig. 16. The left column shows all gas (blue) and star (red) particles inside a cubical region of side length $10h^{-1}$ kpc as well as the gas particles inside a $5h^{-1}$ kpc sphere (green). The right column shows the pressure (upper) and density (lower) for the gas particles along the x -axis using the same colouring scheme.

others ignoring it. Therefore, the fundamental question is, what will different halo finders find when it comes to simulations including baryonic physics?

We found remarkable and excellent agreement between different halo finders when applied to a constrained simulation of the Local Group that includes all the relevant baryonic physics; at least as far as dark matter and stellar content are concerned. However, there appear to be strong discrepancies when it comes to the gas and hence baryon fractions. This result may not be too surprising as both dark matter and stars are particles primarily only feeling gravity (even though stars obviously have a different formation history) whereas gas is also subjected to hydrodynamical forces. It appears that – to properly identify and subsequently analyse and model the gas component in cosmological simulations – halo finders need to take into account the pressure of the gas in the unbinding procedure, especially when dealing with subhaloes containing of order 10,000 or less particles (in total). But we have also seen that some correct accounting of the gas happens in phase-/velocity-space based finders such as ROCKSTAR and STF used here: not all the gas particles inside the radius of the subhalo are considered part of the object; only a residual number of gas particles are kept. In these finders the (hot) gas component is prone to be removed as they inherently use velocity information when grouping and collecting the initial set of particles, whereas configuration space finders only deal with velocities (either kinetic or thermal) in a (post-processing) unbinding procedure.

In summary, the proper treatment of the gas certainly also depends on the actual scientific question to be addressed with the numerical data; any algorithm used for collecting gas particles should carefully consider what type of study they are interested in. For instance, for studies where the X-ray emission from (hot) gas in galaxy clusters is sought, one clearly would not want to remove the majority of the gas (during the unbinding or even before). Further, the differences will certainly become more important for simulations (of subhaloes) with much higher resolution where we expect subhaloes to hang on to their own gas; we have seen here that for this particular data only a few subhaloes still have gas (cf. Fig. 7). But consider gas rich objects at high redshift: for these the baryon fraction would be dominated by the treatment of the gas and is expected to be much larger as stars have not formed yet. This discussion about the proper treatment of the gas (during the unbinding procedure) is akin to debates about unbinding in general: some investigations heavily rely on it (e.g. subhalo dynamics) whereas others can live without it (e.g. gravitational lensing). In any case, the

differences for the three main galaxies investigated here were reassuringly negligible and we conclude that despite subtleties there is in general a fair agreement of “galaxy finders”.

ACKNOWLEDGEMENTS

The work in this paper was initiated at the “Subhaloes going Notts” workshop in Dovedale, UK, which was funded by the European Commissions Framework Programme 7, through the Marie Curie Initial Training Network Cosmo-Comp (PITN-GA-2009-238356). We basically thank all the participants of that meeting for all the stimulating discussions and the great time in general.

AK is supported by the *Spanish Ministerio de Ciencia e Innovación* (MICINN) in Spain through the Ramon y Cajal programme as well as the grants AYA 2009-13875-C03-02, AYA2009-12792-C03-03, CSD2009-00064, and CAM S2009/ESP-1496. He further thanks Christine Corbett Moran for stimulating discussions about halo matching and Marden Hill for the lost weekend. NIL acknowledges a grant from the DFG. PSB was supported by program number HST-AR-12159.01-A, provided by NASA through a grant from the Space Telescope Science Institute, which is operated by the Association of Universities for Research in Astronomy, Incorporated, under NASA contract NAS5-26555. PJE acknowledges financial support from the Chinese Academy of Sciences (CAS), from NSFC grants (No. 11121062, 10878001, 11033006), and by the CAS/SAFEA International Partnership Program for Creative Research Teams (KJCX2-YW-T23). KD acknowledges the support by the DFG Priority Programme 1177 and additional support by the DFG Cluster of Excellence “Origin and Structure of the Universe”. HL acknowledges a fellowship from the European Commissions Framework Programme 7, through the Marie Curie Initial Training Network CosmoComp (PITN-GA-2009-238356).

We like to thank the CLUES team (in particular Stefan Gottlöber, Yehuda Hoffman, and Gustavo Yepes) for granting us access to the simulation used for this comparison project. We also thank Andrea Maccio for kindly providing us with the data of the observed luminosity function (average of MW and M31). And last but not least we thank Volker Springel for useful comments and remarks during the preparation of this work.

REFERENCES

- Abadi M. G., Navarro J. F., Steinmetz M., Eke V. R., 2003, *ApJ*, 597, 21
- Agertz O., Moore B., Stadel J., Potter D., Miniati F., Read J., Mayer L., Gawryszczak A., Kravtsov A., Nordlund Å., Pearce F., Quilis V., Rudd D., Springel V., Stone J., Tasker E., Teyssier R., Wadsley J., Walder R., 2007, *MNRAS*, 380, 963
- Behroozi P. S., Wechsler R. H., Wu H.-Y., 2011, *ArXiv e-prints*
- Blumenthal G. R., Faber S. M., Flores R., Primack J. R., 1986, *ApJ*, 301, 27
- Boylan-Kolchin M., Bullock J. S., Kaplinghat M., 2011a, *ArXiv e-prints*
- Boylan-Kolchin M., Bullock J. S., Kaplinghat M., 2011b, *ArXiv e-prints*
- Brooks A. M., Zolotov A., 2012, *ArXiv e-prints*
- Dayal P., Libeskind N. I., 2012, *MNRAS*, 419, L9
- Devriendt J. E. G., Guiderdoni B., Sadat R., 1999, *A&A*, 350, 381
- Di Cintio A., Knebe A., Libeskind N. I., Brook C., Yepes G., Gottlöber S., Hoffman Y., 2012, *ArXiv e-prints*

- di Cintio A., Knebe A., Libeskind N. I., Yepes G., Gottlöber S., Hoffman Y., 2011, MNRAS, 417, L74
- Dolag K., Borgani S., Murante G., Springel V., 2009, MNRAS, 399, 497
- Doménech-Moral M., Martínez-Serrano F. J., Domínguez-Tenreiro R., Serna A., 2012, MNRAS, 421, 2510
- Duffy A. R., Schaye J., Kay S. T., Dalla Vecchia C., Battye R. A., Booth C. M., 2010, MNRAS, 405, 2161
- Elahi P. J., Thacker R. J., Widrow L. M., 2011, MNRAS, 418, 320
- Frenk et al. C. S., 1999, ApJ, 525, 554
- Gill S. P. D., Knebe A., Gibson B. K., 2004, MNRAS, 351, 399
- Gottlöber S., Hoffman Y., Yepes G., 2010, in S. Wagner, M. Steinmetz, A. Bode, M.M. Müller ed., High Performance Computing in Science and Engineering Vol. 0 of Springer, Constrained Local UniversE Simulations (CLUES). pp 309–323
- Governato F., Zolotov A., Pontzen A., Christensen C., Oh S. H., Brooks A. M., Quinn T., Shen S., Wadsley J., 2012, MNRAS, 422, 1231
- Haardt F., Madau P., 1996, ApJ, 461, 20
- Heitmann K., Lukić Z., Fasel P., Habib S., Warren M. S., White M., Ahrens J., Ankeny L., Armstrong R., O’Shea B., Ricker P. M., Springel V., Stadel J., Trac H., 2008, Computational Science and Discovery, 1, 015003
- Kennicutt Jr. R. C., 1998, in G. Gilmore & D. Howell ed., The Stellar Initial Mass Function (38th Herstmonceux Conference) Vol. 142 of Astronomical Society of the Pacific Conference Series, Overview: The Initial Mass Function in Galaxies. pp 1–4
- Klimentowski J., Łokas E. L., Knebe A., Gottlöber S., Martínez-Vaquero L. A., Yepes G., Hoffman Y., 2010, MNRAS, 402, 1899
- Knebe A., Knollmann S. R., Muldrew S. I., Pearce F. R., et al. 2011, MNRAS, 415, 2293
- Knebe A., Kravtsov A. V., Gottlöber S., Klypin A. A., 2000, MNRAS, 317, 630
- Knebe A., Libeskind N. I., Doumler T., Yepes G., Gottlöber S., Hoffman Y., 2011, MNRAS, 417, L56
- Knebe A., Libeskind N. I., Knollmann S. R., Martínez-Vaquero L. A., Yepes G., Gottlöber S., Hoffman Y., 2011, MNRAS, 412, 529
- Knebe A., Libeskind N. I., Knollmann S. R., Yepes G., Gottlöber S., Hoffman Y., 2010, MNRAS, 405, 1119
- Knollmann S. R., Knebe A., 2009, ApJS, 182, 608
- Koposov S., Belokurov V., Evans N. W., Hewett P. C., Irwin M. J., Gilmore G., Zucker D. B., Rix H., Fellhauer M., Bell E. F., Glushkova E. V., 2008, ApJ, 686, 279
- Libeskind N. I., Knebe A., Hoffman Y., Gottlöber S., Yepes G., 2011, MNRAS, 418, 336
- Libeskind N. I., Knebe A., Hoffman Y., Gottlöber S., Yepes G., Steinmetz M., 2011, MNRAS, 411, 1525
- Libeskind N. I., Yepes G., Knebe A., Gottlöber S., Hoffman Y., Knollmann S. R., 2010, MNRAS, 401, 1889
- Macciò A. V., Kang X., Fontanot F., Somerville R. S., Koposov S., Monaco P., 2010, MNRAS, 402, 1995
- Macciò A. V., Moore B., Stadel J., Diemand J., 2006, MNRAS, 366, 1529
- Mashchenko S., Couchman H. M. P., Wadsley J., 2006, Nature, 442, 539
- Mateo M. L., 1998, ARA&A, 36, 435
- Navarro J. F., Eke V. R., Frenk C. S., 1996, MNRAS, 283, L72
- Oñorbe J., Domínguez-Tenreiro R., Sáiz A., Serna A., 2007, MNRAS, 376, 39
- Okamoto T., Eke V. R., Frenk C. S., Jenkins A., 2005, MNRAS, 363, 1299
- Onions J., Knebe A., Pearce F. R., Muldrew S. I., Lux H., Knollmann S. R., Ascasibar Y., Behroozi P., Elahi P., Han J., Maciejewski M., Merchán M. E., Neyrinck M., Ruiz A. N., Sgró M. A., Springel V., Tweed D., 2012, MNRAS, p. 2881
- O’Shea B. W., Nagamine K., Springel V., Hernquist L., Norman M. L., 2005, ApJS, 160, 1
- Robertson B. E., Kravtsov A. V., Gnedin N. Y., Abel T., Rudd D. H., 2010, MNRAS, 401, 2463
- Romano-Díaz E., Shlosman I., Heller C., Hoffman Y., 2009, ApJ, 702, 1250
- Romano-Díaz E., Shlosman I., Heller C., Hoffman Y., 2010, ApJ, 716, 1095
- Romano-Díaz E., Shlosman I., Hoffman Y., Heller C., 2008, ApJ, 685, L105
- Scannapieco C., Gadotti D. A., Jonsson P., White S. D. M., 2010, MNRAS, 407, L41
- Schewtschenko J. A., Macciò A. V., 2011, MNRAS, 413, 878
- Sommer-Larsen J., Limousin M., 2010, MNRAS, 408, 1998
- Spergel et al. D. N., 2007, ApJS, 170, 377
- Springel V., 2005, MNRAS, 364, 1105
- Springel V., 2010, MNRAS, 401, 791
- Springel V., Hernquist L., 2003, MNRAS, 339, 289
- Springel V., White S. D. M., Tormen G., Kauffmann G., 2001, MNRAS, 328, 726
- Tasker E. J., Brunino R., Mitchell N. L., Michielsen D., Hopton S., Pearce F. R., Bryan G. L., Theuns T., 2008, MNRAS, 390, 1267
- Tissera P. B., Domínguez-Tenreiro R., 1998, MNRAS, 297, 177
- Vazza F., Dolag K., Ryu D., Brunetti G., Gheller C., Kang H., Pfrommer C., 2011, MNRAS, 418, 960
- Vera-Ciro C. A., Helmi A., Starkenburg E., Breddels M. A., 2012, ArXiv e-prints
- Watkins L. L., Evans N. W., An J. H., 2010, MNRAS, 406, 264
- Zolotov A., Brooks A. M., Willman B., Governato F., Pontzen A., Christensen C., Dekel A., Quinn T., Shen S., Wadsley J., 2012, ArXiv e-prints

This paper has been typeset from a \LaTeX file prepared by the author.